HOSTED BY
ELSEVIER

Available online at www.sciencedirect.com
ScienceDirect

Soils and Foundations 65 (2025) 101611

www.elsevier.com/locate/sandf

Technical Paper

Long-distance flow mechanism of gentle slopes under seepage due to liquefaction-induced water film during 2018 Sulawesi earthquake, Indonesia

T. Kokusho [a,*], T. Sawada [b], H. Hazarika [c], Y. Isobe [b]

[a] *Chuo University (Professor Emeritus), Tokyo, Japan*
[b] *IMAGEi Consultant Corporation, Tokyo, Japan*
[c] *Kyushu University, Fukuoka, Japan*

Received 8 October 2024; received in revised form 17 February 2025; accepted 8 March 2025

Abstract

Unprecedented liquefaction-induced slope failure occurred during the 2018 Indonesian Sulawesi earthquake in which more than 2000 people were killed by sliding debris flows in very gentle slopes with a 2 % gradient. In order to clarify the mysterious mechanism of how long-distance debris flows could occur on such gentle slopes, transient seepage analyses were conducted focusing on the impact of a thin water film of a limited horizontal length which was supposed to emerge during liquefaction in a layered soil profile beneath a low-permeability cap layer of the slope influenced by stationary seepage. Consequently, the water film was found to play a key role in transmitting higher pressure head to the tip at a lower elevation with a marginal head loss, leading to the downslope extension of the water film and associated boiling failure in the cap layer. The water film that formed during liquefaction was significant in realizing the long-distance flows down the gentle slopes during and even after liquefaction as long as the water film was sustained. This mechanism should be newly recognized as a serious threat to a society due to liquefaction in gentle slopes during strong earthquakes.

Keywords: Liquefaction-induced slope failure; Long-distance flow; Water film; Transient seepage analysis; Layered soils

1. Introduction

An unprecedented liquefaction-induced calamity in recent history occurred in Palu City, Sulawesi Island, Indonesia during the 2018 Sulawesi earthquake of $M_w = 7.5$, in which more than 2000 people were buried to death by sliding debris flows traveling a long distance down very gentle slopes with an approximate gradient of 2 %, as reported in detail by JICA (2019), Okamura et al. (2020), Kiyota et al. (2020), Hazarika et al. (2020), and Rohit et al. (2021, 2023). The peak horizontal acceleration recorded was 3.3 m/s^2. The affected areas were fluvial plains along a narrow valley carved by the Palu River running north between mountain ridges 1000 m in height. Four areas of more or less several km^2 each, named Balaroa, Petobo, Jono Oge, and Sibalaya, underwent long-distance flow slides of a few km in length in total: Balaroa to the west and the other three to the east of the valley and the earthquake fault.

The slides started at the upper parts of the sandy fluvial plains where gravelly alluvial fans came down from steep mountain slopes. Even before the earthquake, groundwater was supposed to have flowed steadily down from the fans to the gently inclined fluvial plains, presenting stationary seepage flows, shallow groundwater levels, and local artesian pressures. Furthermore, an unlined agricultural

* Corresponding author at: 46-5-1504 Senju-Asahi-cho, Adachi-ku, Tokyo 120-26, Japan.
E-mail address: koktak@ad.email.ne.jp (T. Kokusho).

https://doi.org/10.1016/j.sandf.2025.101611
0038-0806/© 2025 Japanese Geotechnical Society. Published by Elsevier B.V.

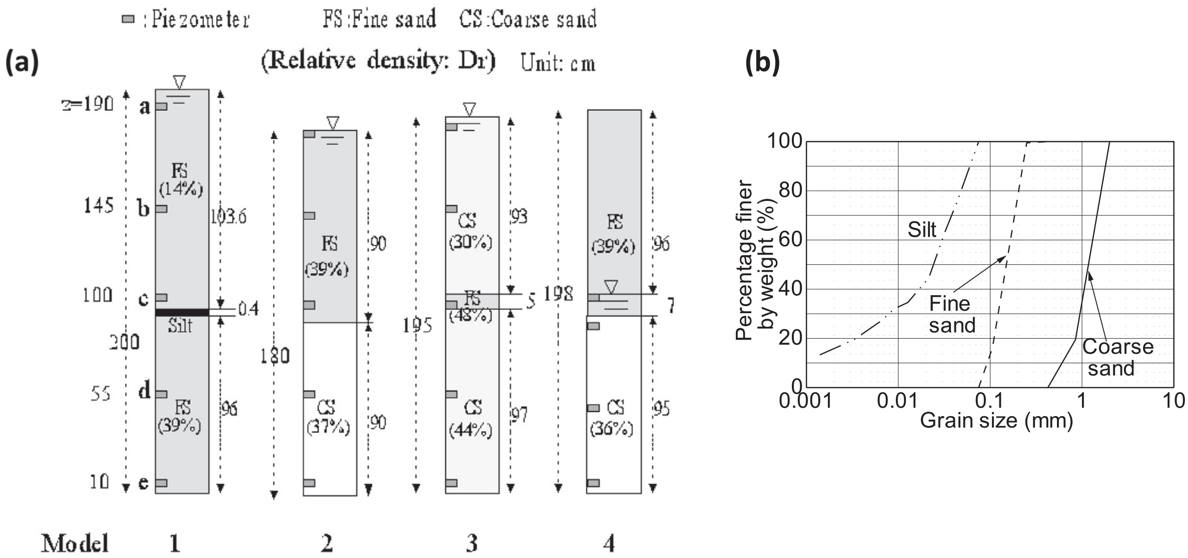

Fig. 1. (a) Four layered soil models employed in tube tests and (b) grain size curves of soil materials employed in the tests.

irrigation channel, passing through the foot of the fans, is suspected to have served as an additional groundwater source to the three slides on the east side of the valley.

Many accounts have been gathered from residents who witnessed that the slides started belatedly, about one minute after the shaking of the strong earthquake had ceased, depending on different slides and different interviewees (Okamura et al. 2020; Hazarika et al. 2020). The speed of the sliding debris, constituting the cap layers of the slopes, was estimated to be almost constant, at 15 ~20 km/h, based on a video taken by a survivor at Jono Oge (Kiyota et al. 2020). Due to the constant speed of the sliding debris, it may be possible to estimate the shear resistance exhibited during the sliding using the principle of energy balance during earthquakes (Kabasawa & Kokusho 2004; Kokusho 2017). In other words, in an infinitely long slope model, the following equation holds:

$$E_{gr} + E_{eq} = E_{dp} + E_k \tag{1}$$

where four energies are involved: gravitational energy $E_{gr} = \rho g D \delta \tan\theta$, earthquake energy E_{eq}, dissipated energy due to sliding $E_{dp} = (\rho g D - u_0)\cos\theta \tan\phi \times (\delta/\cos\theta) = (\rho g D - u_0)\delta \tan\phi$, and kinetic energy $E_k = \rho D \dot{\delta}^2/2$. Here, ρg is the unit weight, D is the thickness, δ is the horizontal displacement of the sliding debris, ϕ is the equivalent friction angle, θ is the slope angle, u_0 is the initial pore pressure at the slip plane, and $\dot{\delta}$ is the horizontal sliding speed.

Eq. (1) is changed to the following incremental form if $\Delta E_{eq} = 0$ or the earthquake motion has already subsided:

$$\Delta E_{gr} = \Delta E_{dp} + \Delta E_k \tag{2}$$

Here, the kinetic energy increment is zero: $\Delta E_k = (\rho D/2)\Delta\left(\dot{\delta}^2\right) = \rho D \dot{\delta} \cdot \Delta\dot{\delta} = 0$, considering that the sliding velocity of the debris observed in the video was constant ($\Delta\dot{\delta}$=0). Then, $\Delta E_{gr} = \Delta E_{dp}$ holds, implying that the same amount of energy supplied by gravity ΔE_{gr} was dissipated during the sliding of the slopes by ΔE_{dp} in the given time increment. This leads to $\rho g D \delta \tan\theta = (\rho g D - u_0)\delta \tan\phi$ and further to

$$\tan\phi = \frac{\rho g D}{(\rho g D - u_0)} \tan\theta \tag{3}$$

If the water table is at the ground surface, then $\rho \rightarrow \rho_{sat}$, $u_0 \rightarrow \rho_w g D$. If it is at the bottom of the sliding debris, then $u_0 \rightarrow 0$, leading, respectively, to

$$\tan\phi = \frac{\rho_{sat}}{(\rho_{sat} - \rho_w)} \tan\theta \; or \; \tan\phi = \tan\theta \tag{4}$$

If $\tan\theta = 0.02$ is assumed, then $\tan\phi = 0.045$ or 0.02, yielding $\phi \approx 2.6^\circ$ or 1.1°, correspondingly, indicating that an extremely small friction angle was actually mobilized.

The maximum continuous flow distance of the debris was confirmed to be about 300 m in Balaroa, 1100 m in Petobo, several hundred meters in Jono Oge (Kiyota et al. 2020), and 360 m at the longest in Sibalaya (Okamura et al. 2020). The soils of the fluvial plains at the four locations that underwent such long-distance flow slides have been reported without exception to be loosely deposited gravelly, sandy, silty, and organic soils mutually interlayered. According to Kiyota et al. (2020), evidence of liquefaction, such as sand ejecta, was observed here and there in the upslope zones of these long-distance flows. Moreover, a soil profile was also observed from the surface down to GL.-4 m at the main scarp of the upper ends in Petobo and Jono Oge, alternating between layers of silty, sandy, and gravelly soils parallel to the ground surface. At the top portion of the Jono Oge slide, numerous cracks appeared. They extended to depths of around 2.5 m, where a clear soil stratification, composed of organic soil followed by interlayers of silty clay, silty sand, and gravelly sand down to GL.-1.5 m, was observed (Hazarika et al. 2020).

It was followed by loose liquefiable layers where the SPT N-values converted by DCPTs (dynamic cone penetration tests) were below 5. Okamura et al. (2020) conducted detailed trench investigations at various points along the slope of the Sibalaya flow slide. They identified the liquefied layers of gravelly sand which were overlain by low-permeability silty and paddy soils at the ground surface. The DCPTs conducted at Petobo and Jono Oge disclosed that soils were loose with converted SPT N-values mostly below 5 at least down to the depth of 5 m from the pre-slide ground surface (Kiyota et al. 2020; Hazarika et al. 2020).

Thus, the unprecedented long-distance flow slides in the very gentle slopes seem to be undoubtedly attributable to the liquefaction of the loosely deposited fluvial soils composed of interlayered silt, sand, and gravel, and to have started somewhat belatedly due to the long-period motion of the M_w7.5 nearfield earthquake. Then, it is quite reasonable to estimate that the layers of the silty, sandy, and gravelly soil strata may have generated water interlayers (NRC report 1985) or water films (Kokusho 2000) beneath the less permeable upper layers because of the pore water migration or void redistribution during intensive liquefaction, as suggested in the three reconnaissance papers addressed above and as discussed by Mason et al. (2021). The water films are likely to have caused the instability of the overlying cap layers due to the literally zero shear resistance, as substantiated in the already mentioned ϕ-values back-calculated using the recorded video. If they had formed continuously at certain lengths, they would surely be responsible for flow failures even in gentle slopes. Such a phenomenon seems to have actually occurred in Niigata City, although not so extensively, during the 1964 Niigata earthquake, wherein the ground surface slid downslope by 4 m maximum along almost flat land with a gradient of less than 1 % (Kokusho & Fujita 2002). Furthermore, it has been pointed out that most sandy layers, natural or manmade, are normally interlayered with multiple sublayers of different permeabilities (Kokusho 2003).

However, if the soil profiles in situ for Palu and other alluvial sites are carefully observed, it will be confirmed that the interlayered soil profiles are not so continuous in long horizontal distances, but are more or less randomly stratified. Hence, it is beyond a doubt that water films can never be generated so continuously and smoothly as to facilitate long-distance flows of surface soils 100 m in length. Hence, the water film mechanism alone, although it contributed to the initial destabilization in the gentle slopes locally, cannot explain why such slope slides of a limited length could develop over a much longer distance, leading to such a huge loss of human lives. Thus, the unprecedented case history in Indonesia poses a great mystery and serious challenge for geotechnical investigators in terms of clarifying the mechanism, as no clear understanding of how such long flow slides could occur on such super-gentle slopes has been provided thus far in the realm of geomechanics.

In the following, a short visit will firstly be made to previous research findings on the water film generation mechanism in layered soils during liquefaction. Then, a numerical study will be conducted on a slope model simplified from the Palu slopes under the effect of stationary seepage flow from upper slopes to explore how the initial slides of finite length, triggered by liquefaction-induced water films, could propagate in downslopes and develop into such long-sliding devastation. For that purpose, a series of transient seepage analyses will be conducted to simplify the complicated liquefaction and water film generation processes on a gently inclined slope.

2. Review of liquefaction-induced water film mechanism

The possibility of the formation of water interlayers was firstly suggested and discussed conceptually in relation to the cause of the Lower San Fernando earth dam failure during the 1971 San Fernando earthquake (Seed 1987) in terms of liquefaction-induced slope slides in the NRC report (1985) in the USA. In order to demonstrate how these water interlayers were formed during liquefaction, one-dimensional column tests on saturated sands were firstly conducted by Elgamal et al. (1989) wherein a silty soil was sandwiched between the interlayers. As a theoretical study, Boulanger and Truman (1996) conducted triaxial tests to investigate the void redistribution mechanism of loose sand deposits responsible for generating a water interlayer beneath a low-permeability layer.

Concerning the soil layering which may form water interlayers or water films in actual soil deposits, Kokusho & Kojima (2002) carried out sieving tests on thin slices seamlessly sampled at trenches in the field. They found that the particle size alternated frequently along depth, particularly in hydraulically filled manmade deposits, but also in natural fluvial deposits as well. Even in apparently uniform sandy deposits, the permeability in the vertical direction tended to vary considerably because the particle size curves were frequently changing.

Based on such field data, 1D column tests were conducted for simplified one-dimensional models comprising multiple layers conceivable under the field conditions depicted in Fig. 1. The four layered models (Models 1 to 4) shown in Fig. 1 (a) were tested. The soil materials of the grain size curves given in Fig. 1 (b) were rained into transparent acrylic tubes filled with water from the top to make loose soil layers with the relative densities indicated in Fig. 1 (a). Video images of these 1D column tests are available at https://kokasahi.com/koktak/ (accessed Dec. 2024).

Model 1 consisted of uniform fine sand, 200 cm in depth, sandwiching a silt seam of non-plastic silt, 4 mm in thickness, in the middle (96 cm from the bottom), beneath which a water film appeared immediately after full liquefaction that was triggered by the hammer impact, as seen in Fig. 2 (a). The water film grew thicker in 20 s, up to the peak of 1 cm, and was sustained for 200 s, much

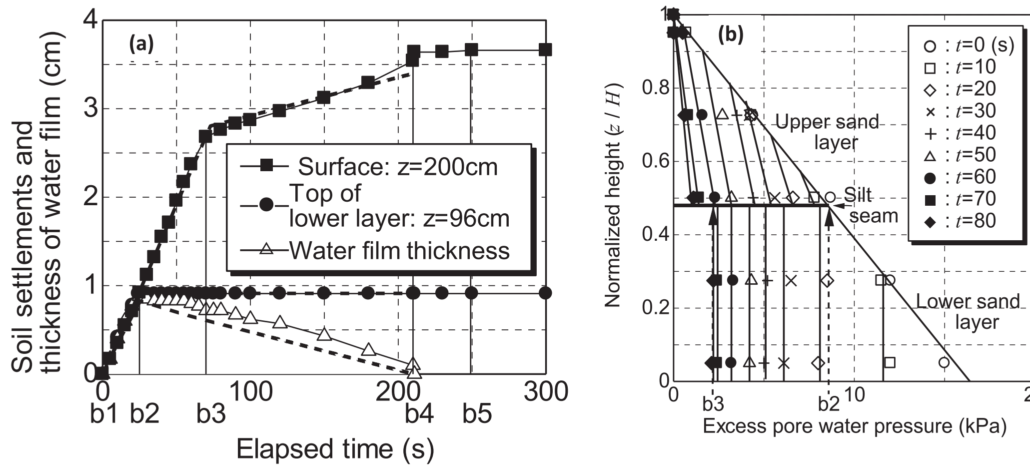

Fig. 2. (a) Settlement and water film thickness versus time after instantaneous liquefaction, and (b) excess pore water pressure profile changing over time.

longer than the liquefaction. The associated time-dependent variations in the excess pore water pressure along depth are illustrated in Fig. 2 (b). The sand was fully liquefied with the hydraulic gradient of $i = i_{cr} \equiv (\rho_{sat} - \rho_w)/\rho_w$, where i_{cr} is the critical hydraulic gradient, ρ_{sat} is the saturated soil density, and ρ_w is the water density. With the passage of time, the excess pore water pressure decreased from the bottom of the lower and upper sand layers, individually, where sand particles resettled and recovered from liquefaction. The corresponding pressure was evidently linear along depth in the upper layer, indicating the clear influence of upward seepage flow from the water film, while it remained constant versus depth in the lower layer below the water film, reflecting that the liquefaction had already subsided there. It is noted that the constant pressure in the lower post-liquefaction layer should be kept identical to the initial effective overburden stress at the silt seam if it is under field conditions, although it falls to a much lower value with time due to the skin friction between the tube wall and the sand (Kokusho and Kojima 2002).

Model 2 in Fig. 1 (a) consisted of the fine sand and coarse sand shown in Fig. 1 (b) in the upper and lower sand layers, respectively, 90 cm in thickness each. In this case, in place of a stable water film, fierce turbulence occurred at the boundary due to the excess pore water coming out of the lower coarse sand, staying only for a few seconds near the boundary, and then fading away.

Model 3 in Fig. 1 (a) consisted of three layers: upper and lower coarse sand and middle sandwiched fine sand, where a stable water film appeared beneath the fine sand in this case. Time-dependent variations in the settlement and the water film thickness indicated a strong similarity to Model 1 in Fig. 1 (a), although they were much shorter in this case because of the higher permeabilities.

Model 4 in Fig. 1 (a) was almost identical to Model 2, except that the water table stayed in the middle of the upper fine sand layer. In this case, a stable water film formed near the boundary of the two layers presumably due to the lower permeability of the unsaturated layer. This may imply that a water film can form even without a sandwiched layer if the groundwater table is above the liquefied layer.

The series of column tests yielded the following findings (Kokusho and Kojima 2002) which ought to be referred to when estimating what may have happened on the Palu slope slides.

- If loose sandy deposits liquefy, water films tend to show up shortly after the onset of liquefaction beneath the layered boundaries where the upper layer is less permeable than the lower one because such soil conditions are prevalent in situ.
- After a water film is formed at the top of the liquefied layer, it tends to greatly outlive the liquefaction itself until all the water temporarily stored there has slowly migrated through the overlying and less permeable soils toward the ground surface.
- Once the water film has formed, the upper layer is disposed to a hydraulic gradient due to upward seepage flow from the water film, while the hydraulic gradient is zero in the lower layer if liquefaction has already ceased.
- The life span of a water film is quite variable, from only seconds to hours, depending on the soil profiles and the permeabilities of the overlying soils.

Water films in sloping terrains will contribute to decreasing the soil stability even in very gentle slopes, because of their near-zero shear resistance. After the 1D column tests, two-dimensional model shaking table tests were conducted under one gravity (Kabasawa & Kokusho 2004; Kokusho 2003), as illustrated in Fig. 3 (a), to demonstrate how liquefaction-induced water films will lead to slope instability. Clean fine sand was rained in water to make a two-dimensional saturated loose sand slope in a rectangular lucite soil box in which an arc-shaped silt seam (of plastic or non-plastic silt), with an

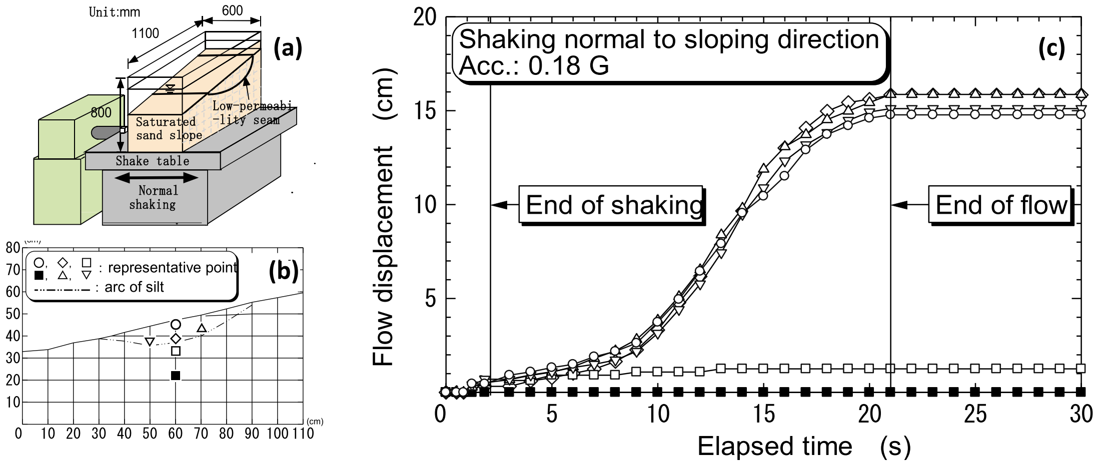

Fig. 3. (a) Shaking table tests on saturated slope model, (b) slope section sandwiching arc of silt seam, and (c) time histories of flow displacements at representative points.

average thickness of 4 mm, was sandwiched as illustrated in Fig. 3 (b). Then the model, completely submerged under water, was subjected to sinusoidal shaking perpendicular to the sloping direction and the flow movement was observed through the transparent side wall. Video images of the 2D shaking table tests are available at https://kokasahi.com/koktak/ (accessed Dec. 2024).

Similar 2D model shaking table tests were conducted in a large centrifugal testing machine, in which a trapezoidal saturated sand slope with a silt seam was shaken (Kulasingam et al. 2004; Malvick et al. 2005). A strong effect of the seam on the sliding deformation was analogously found, although the process was completed in 1/38 the real time under centrifugal gravity.

Some of the test findings that help understand what has possibly happened in the Palu slide are:

- The soil mass above the silt arc started to flow dramatically along a continuously formed water film beneath the seam slightly after the end of shaking, as depicted in Fig. 3 (c), while only minor lateral displacement took place during shaking in a uniform sand slope without the silt seam.
- It took some time from the end of shaking until the initiation of the post-shaking slide for the water film to be thick enough for the shear resistance along the sliding plane to become lower than the driving force of the sliding block (Kabasawa & Kokusho 2004).

However, unlike the 2D model tests, in which a water film was deliberately formed continuously beneath the silt arc, water films that supposedly appeared during the Palu slides could never be as continuous as hundreds of meters long. It may not be difficult to come to such conclusions from the field trench observations in the Palu slides and other sites in general. Instead, the water films may have been interrupted or dispersed into tiny branches at shorter distances toward the downslope direction because of poor horizontal continuity. Nonetheless, the slide did occur continuously on a huge scale, driving immense soil debris flows more than hundreds or thousands of meters, resulting in the death of thousands of residents downslope. It is believed, therefore, that there is a yet undiscovered mechanism that enhances long-distance slope sliding.

It is the present authors' view that the key to uncovering this mysterious mechanism in the field is somehow associated with the seepage water steadily flowing downslope combined with water films. Water films of a certain horizontal length in a gently sloping ground under stationary seepage flow are expected to serve as water passages, wherein the groundwater can flow much more easily with minimal head loss than the ambient water flowing down through soil skeletons with normal head loss. This view was the motivation for conducting the numerical analysis in this paper.

In order to numerically reproduce, as realistically as possible, what happened in this event, very challenging numerical techniques, beyond conventional ones, would be required by employing the DEM (discrete element method) or SPH (smooth particle hydrodynamics) to simulate earthquake-induced liquefaction, water film generation, and subsequent long-distance slope sliding. Instead, a transient seepage analysis will be carried out here as an approximation, focusing on the effect of a water film during/after liquefaction, under the influence of steady seepage flow, to explore the key mechanism of the long-distance failure propagation in gentle slopes.

3. Analytical slope model

Fig. 4 (a) shows a typical cross section of the slope model, with a 2 % gradient and a horizontal length of 200 m, cut out from the uppermost part of the Palu slope sliding. In the 2D model, orthogonal x-z axes are defined, where the x-axis extends rightward from the model's left boundary and the vertical z-axis extends downward from

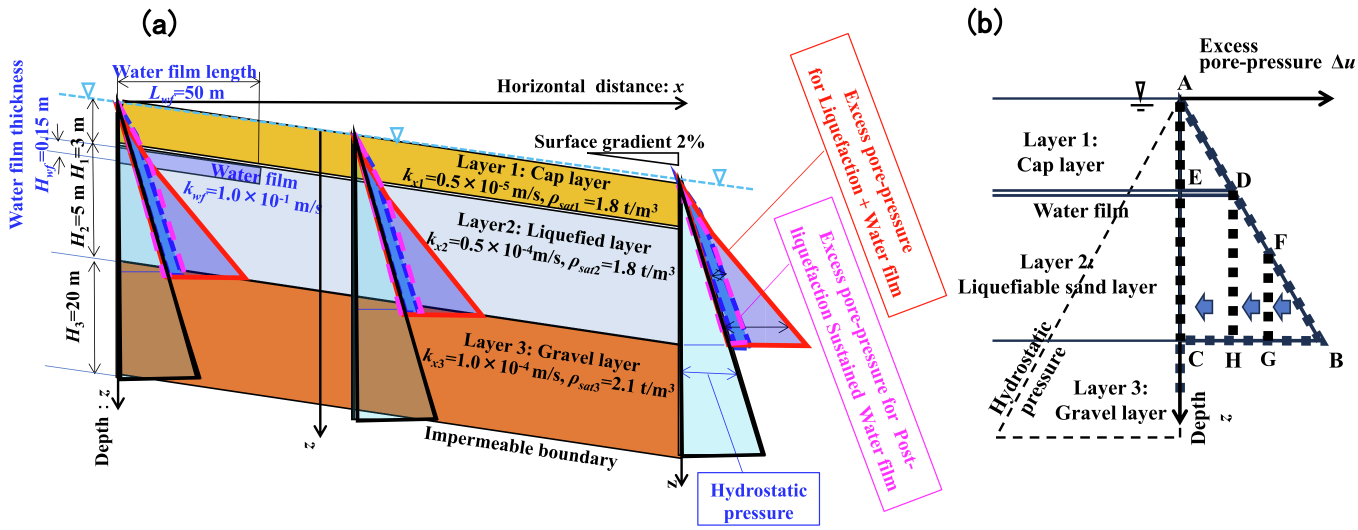

Fig. 4. Schematic gentle slope model under stationary seepage flow comprising three layers: cap layer, liquefiable layer, and gravelly layer, where thin water film is instantaneously introduced, together with initial water pressure given inside as well as lateral boundaries.

the slope surface at arbitrary x-coordinates. A potential water flow analysis under 1-g gravity is performed using these orthogonal axes on the 2 % slope model, where the water table is consistently maintained at the ground surface. This configuration induces a 2 % hydraulic gradient throughout the analysis.

The model consists of three layers simplified from field trenching investigations in Palu: Layer 1 is a non-liquefiable cap layer, with a thickness of 3 m and horizontal permeability of $k_{x1} = 0.5 \times 10^{-5}$ m/s, underlain by Layer 2 of liquefiable sand, with a thickness of 5 m and horizontal permeability of $k_{x2} = 0.5 \times 10^{-4}$ m/s, and then Layer 3 of non-liquefiable gravel, with a thickness of 20 m and horizontal permeability of $k_{x3} = 1.0 \times 10^{-4}$ m/s. The vertical permeability k_z of each layer is assumed to be half of the horizontal permeability k_x. As mentioned previously, the ground water table is postulated to coincide with the ground surface, although the water tables observed after the quake were lowered presumably to reflect the slope failures. This indicates that the entire slope section was fully saturated by the steady-state horizontal seepage flow with the hydraulic gradient of $i_x = 2$ %. Even though, from place to place, these conditions may deviate more or less from reality, they will not deviate the basic trends of the results.

During the earthquake shaking, excess pore pressure Δu is supposed to build up 100 % all over the 5-m-thick liquefiable layer (Layer 2), while that in the underlying gravel layer (Layer 3) remains at zero because of higher liquefaction resistance. As already observed in the results of the 1D tests, given in Fig. 2 (a), a water film, if generated, is supposed to appear beneath the cap layer with lower permeability at an earlier stage of liquefaction. Accordingly, excess pore pressure Δu is expected to be maintained in Layer 2 as the dashed lines forming EDHC in Fig. 4 (b) even after the liquefaction-induced excess pore-pressure has subsided. It is noted that, not only in Layer 2, but also in Layer 1, pressure ADE $\Delta u = (\rho_{sat} - \rho_w)gz$ builds up due to upward seepage flow from the underlain layer. Then, Δu tends to gradually recede, recovering from the initial ADBCE to AFGCE and farther below, as observed in the model tests in Fig. 2 (b).

In order to numerically explore the effect of a water film on the water pressure distribution in the slope, a thin layer of water film is instantaneously introduced at the top of the liquefied layer, as illustrated in Fig. 4 (a), at the very beginning of the transient seepage analysis. Although the length of the horizontal water film may vary and be difficult to determine, it is tentatively set as $L_{wf} = 50$ m (from $x = 0$ to 50 m) in the model. The effect of this important parameter will be discussed later on.

As for the thickness of the water film layer, it may be reasonably assumed to be equivalent to the ultimate liquefaction-induced settlement. Since the post-liquefaction settlements are known to be 3 ~ 5 % of the liquefied layer thicknesses, according to previous liquefaction case histories (e.g., Kokusho 2017), the value of 5.0 m × 0.03 = 0.15 m was chosen here.

In the model slope in Fig. 4 (a), excess pore pressure Δu and vertical hydraulic gradient i_z during the full liquefaction can be formulated in Layers 1, 2, and 3, respectively, as follows:

$$\left.\begin{array}{l} \Delta u = (\rho_{sat1} - \rho_w)gz: \quad 0 \le z \le H_1 \\ \Delta u = (\rho_{sat1} - \rho_w)gH_1 + (\rho_{sat2} - \rho_w)g(z - H_1): \quad H_1 \le z \le H_2 \\ \Delta u = 0: \quad H_2 \le z \le H_3 \end{array}\right\} \tag{5}$$

$$\left.\begin{array}{l} i_z = \frac{\partial}{\partial z}\frac{\Delta u}{\rho_w g} = (\rho_{sat1} - \rho_w)/\rho_w: \quad 0 \le z \le H_1 \\ i_z = \frac{\partial}{\partial z}\frac{\Delta u}{\rho_w g} = (\rho_{sat2} - \rho_w)/\rho_w: \quad H_1 \le z \le H_2 \\ i_z = 0: \quad H_2 \le z \end{array}\right\} \tag{6}$$

Here, H_1, H_2, and H_3 are the thicknesses of Layers 1, 2, and 3, respectively, ρ_{sat1} and ρ_{sat2} are the soil densities of Layers 1 and 2, respectively, ρ_w is the water density, and

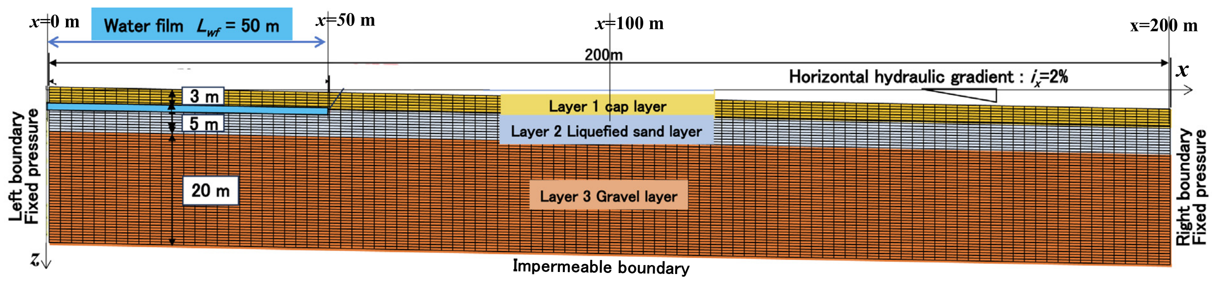

Fig. 5. Cross section of real vertical/horizontal scale discretized FEM model, 200 m by 28 m, with 2 % gradient, comprising cap layer, liquefied layer, and gravel layer, with 50-m-long water film appearing at top of liquefied layer on upslope side.

g is the acceleration of gravity. The water film forms between Layers 1 and 2, and presents a vertical hydraulic gradient of $i_z = (\rho_{sat1} - \rho_w)/\rho_w$ which causes upward seepage flow in the cap layer.

If liquefaction is terminated and the water film is still sustained, the corresponding excess pore pressure Δu and hydraulic gradient i_z are expressed as follows:

$$\left.\begin{aligned} &\Delta u = (\rho_{sat1} - \rho_w)gz: \quad 0 \le z \le H_1 \\ &\Delta u = (\rho_{sat1} - \rho_w)gH_1: \quad H_1 \le z \\ &\Delta u = 0: \quad H_2 \le z \end{aligned}\right\} \tag{7}$$

$$\left.\begin{aligned} &i_z = \frac{\partial}{\partial z}\frac{\Delta u}{\rho_w g} = (\rho_{sat1} - \rho_w)/\rho_w: \quad 0 \le z \le H_1 \\ &i_z = 0: \quad H_1 \le z \end{aligned}\right\} \tag{8}$$

The excess pore pressure distributions by Eqs. (5) and (7), corresponding to the conditions of liquefaction with a water film and post-liquefaction with a sustained water film, respectively, are illustrated in Fig. 4 (a). In formulating the excess pore pressure Δu in Eqs. (5) and (7), a level ground is assumed instead of a 2 % sloping ground due to the minimal gradient. Additionally, determining the liquefaction-induced excess pore pressure in a sloping ground would require that an effective stress liquefaction analysis be performed in advance, which is beyond the scope of this approximate evaluation.

Fig. 5 shows the 1:1 vertical/horizontal scale FEM model of the 2 % gradient slope. The discretized FEM model consists of a total of 5700 rectangular elements, with dimensions of 2.0 m by 0.5 m, except for 100 thin elements with dimensions of 2.0 m by 0.15 m, to accommodate the water film beneath the 3-m-thick cap layer. In other words, the far-left of the thin elements, 50 m in length ($x = 0$ to 50 m selectively), is supposed to represent the water film with the horizontal permeability coefficient of $k_{wf} = 1.0 \times 10^{-1}$ m/s, while all the other elements on the right side have the same permeability as the liquefied layer. This value (2×10^3 times the liquefiable sand layer $k_x = 0.5 \times 10^{-4}$ m/s) seems conservative and could be much larger if the permeability is assumed to be roughly proportional to the square of the soil particle diameters or the soil void diameters (water film thickness/mean grain size of soil)^2 = (150 mm/0.2 mm)^2 = 560 $\times$ 10^3. However, it may not be unrealistic if other reverse effects are considered, such as the ruggedness and zigzaggedness of the water film, to make the permeability considerably smaller.

In the analysis, the excess pore pressures in Eqs. (5) and (7) are prescribed as the initial conditions for all the elements as well as at the side boundaries of the model. Namely, all the developments expected to occur during full liquefaction, including 100 % pore-pressure buildup and subsequent water film generation, are assumed to take place instantaneously at the beginning of the transient seepage analysis with $t = 0$ as the initial condition inside and at the lateral boundaries. Meanwhile, the base of the model is assumed to always be impermeable.

4. Analytical procedure

In a pre-earthquake situation, a stationary downslope seepage flow is firstly reproduced with hydrostatic pressure given to the right/left boundaries of a simplified slope model with a 2 % gradient. During the earthquake shaking, the pore pressure is supposed to build up 100 % all over the 5-m-thick liquefiable sand layer, while the underlying gravel layer remains unchanged because of higher liquefaction resistance. The water film is assumed to appear in earlier stages of liquefaction. In order to mimic this situation, transient seepage analyses are conducted with the initial excess pore pressure distribution corresponding to the following two conditions: (1) liquefaction combined with a water film, and (2) post-liquefaction with a sustained water film, as formulated in Eqs. (5) and (7), respectively, and also depicted in Fig. 4 (a). In other words, the pressure distribution during liquefaction is approximated by the transient seepage analysis in this research despite the basic difference from the liquefaction behavior, because the goal of this research is not to replicate the exact pressure buildup during liquefaction, but to explore the role of the water film in a liquefied gentle slope.

With that objective in mind, identical transient seepage analyses are conducted for two cases here: with and without a water film, under the same background pressure distributions mimicking liquefaction and the stationary seepage flow. The difference between the analytical results, under otherwise exactly the same conditions, will single out the effect of the water film on the pressure variation by canceling out the somewhat deviating values created in the transient seepage analysis.

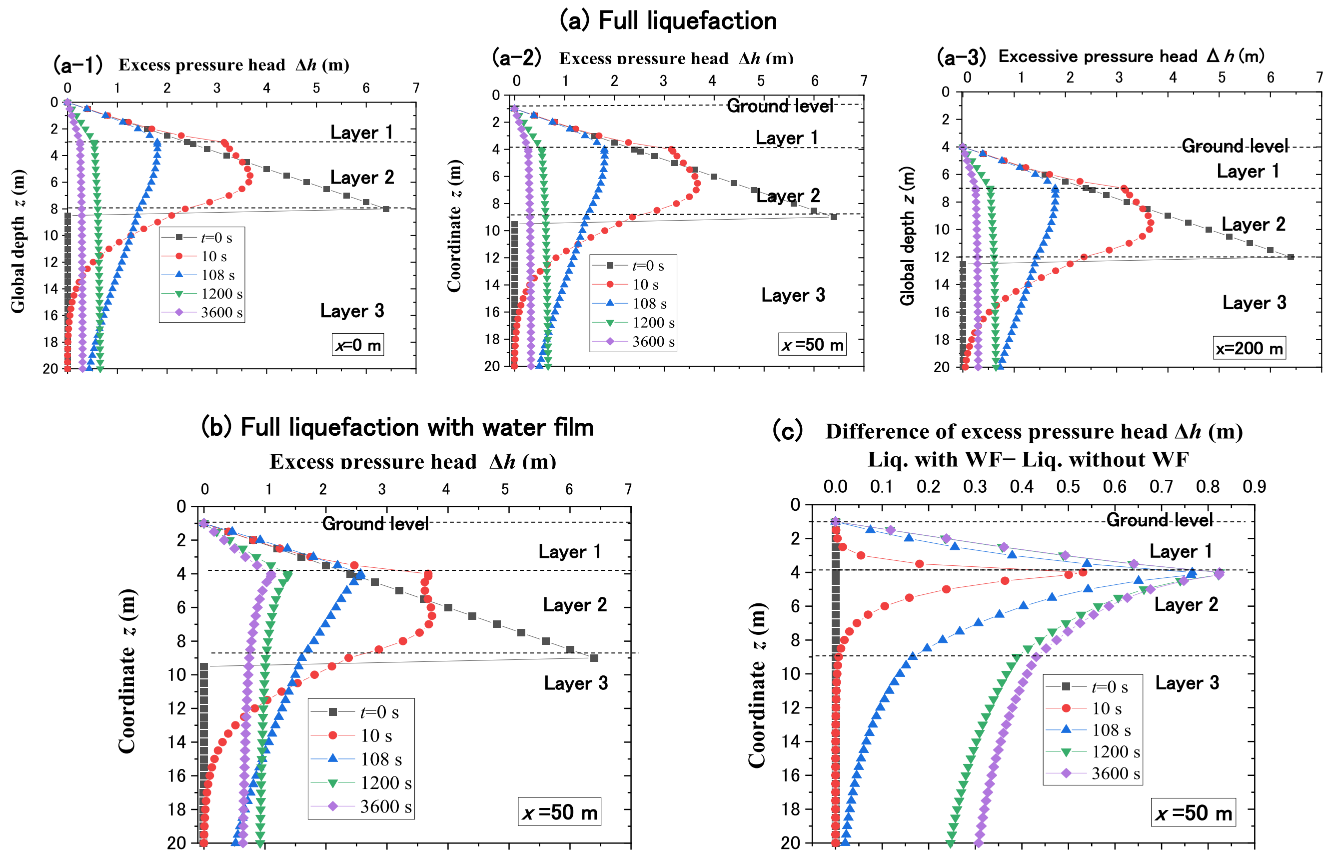

Fig. 6. Depth-dependent distributions of excess pressure heads for elapsed time of $t = 0$ ~3600 s (1 h) obtained by transient flow analyses: (a) full liquefaction at $x = 0$, 100, and 200 m, (b) full liquefaction with water film at $x = 50$ m, and (c) (a)-(b) at $x = 50$ m.

5. Analytical results

The computer program used here is commercially available software (Soil Plus Flow Ver. 14.0.0, https://www.engineering-eye.com/SOILPLUS/features/index.html#anc_02) which was developed based on the theoretical formulation by Akai et al. (1977, 1979).

At the start, a stationary seepage analysis was conducted to confirm that the hydrostatic pressure given at the up/down-slope boundaries was uniformly distributed all over the section of the model given in Fig. 5. The associated horizontal seepage velocities v_x of the downslope water flow were obtained as $v_{x1} = 0.1 \times 10^{-6}$ m/s, $v_{x2} = 1.0 \times 10^{-6}$ m/s, and $v_{x3} = 2.0 \times 10^{-6}$ m/s in Layers 1, 2, and 3, respectively, which are coincidental with the simple formula $v_x = -k_x i_x$ with $i_x = 0.02$.

As previously mentioned, two scenarios are analyzed using transient seepage analyses: (1) full liquefaction with a water film, and (2) post-liquefaction with a sustained water film. These two cases are considered because the impact of a water film is not confined to the liquefaction phase, but extends into the post-liquefaction stage, where the water film persists even after liquefaction, as demonstrated by the laboratory tests depicted in Figs. 2 and 4 (b).

(1) Transient Seepage Analysis for Liquefaction with Water Film

In preparation for investigating the effect of a water film on the pressure distributions during liquefaction in gentle slopes under the influence of stationary seepage flow, a transient seepage analysis was firstly conducted on the model in Fig. 5 by prescribing the initial pressure heads appearing in Fig. 4 (b), in area ADBCE, corresponding to full liquefaction in Layer 2 and upward seepage flow in Layer 1 all over the model elements and the lateral boundaries.

Fig. 6 (a) shows the distributions of excess pressure heads Δh (total pressure − hydrostatic pressure) versus depth z calculated for three vertical lines at $x = 0$ m (the left boundary), $x = 50$ m (the tip of the water film), and $x = 200$ m (the right boundary). To obtain these results, a two-step analysis was conducted on the same model in Fig. 5 whose respective boundary/initial conditions are different. In the first step, the excess pressure in Eq. (5) is applied to all elements as the initial condition, and to the two lateral boundaries as a fixed condition that remains unchanged throughout the entire analysis. In the second step, the variation in the time-dependent pressure, calcu-

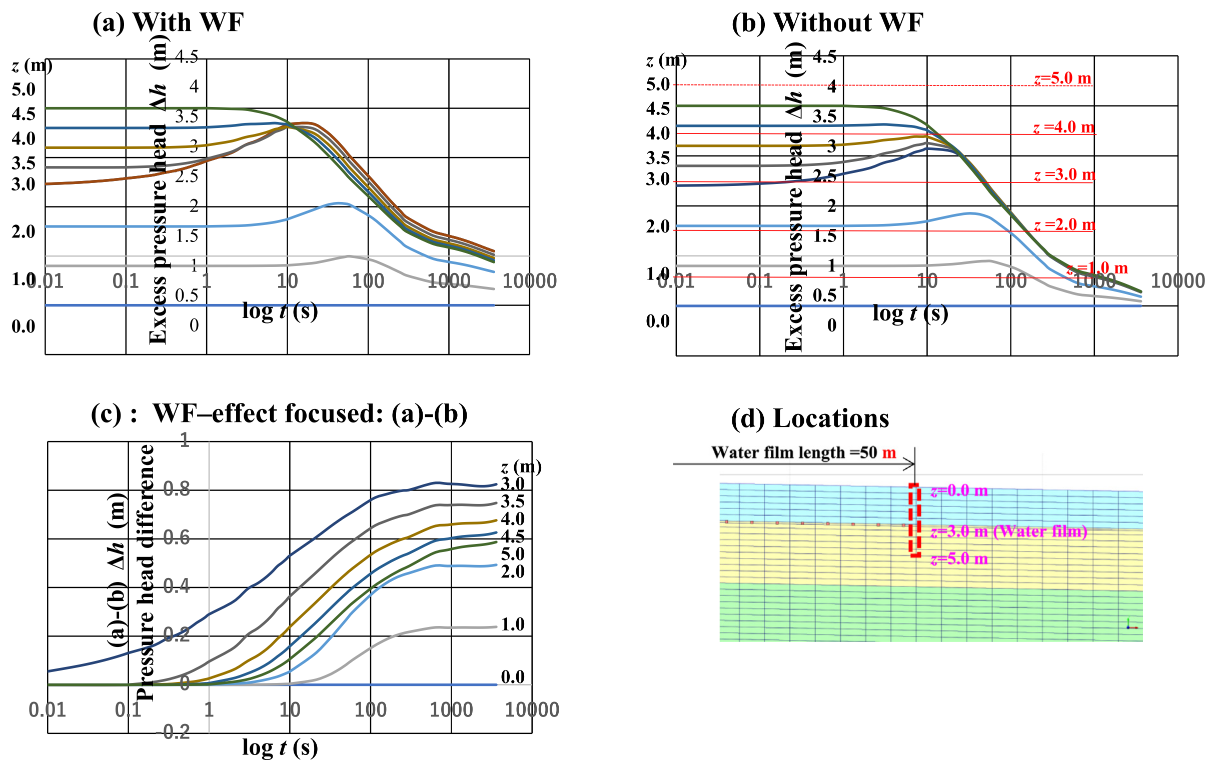

Fig. 7. Variations in excess pressure head for elapsed times of $t = 0$ ~3600 s obtained by transient flow analysis during liquefaction along vertical line at $x = 50$ m, z = 0.0 − 5.0 m: (a) with WF, (b) without WF, (c) subtraction of (a)–(b), and (d) locations of calculation points.

lated in the first step along depth ($x = 100$ m at the centerline is chosen here), is applied as the time-dependent boundary condition at the lateral boundaries, while the pressures in Eq. (5) are assigned to all the elements as the initial condition. This two-step calculation was necessary to replicate the uniform excess pore pressure distribution mimicking the full liquefaction conditions throughout the slope model, including the lateral boundaries.

The top three graphs in Fig. 6 (a), namely, (a-1), (a-2), and (a-3), show excess pressure heads Δh versus depth z plots for the elapsed time of $t = 0 \sim 3600$ s, thus obtained in the second calculation step. Exactly the same Δh-values were obtained with no visible differences among the three vertical lines, namely, $x = 0$, 50, and 200 m, indicating that this transient seepage analysis can reproduce identical pressure distributions all over the slope throughout the time. The calculated pressures start from the initial condition corresponding to the full liquefaction prescribed by Eq. (5), and gradually decrease with time in the liquefied layer (Layer 2) and the cap layer (Layer 1), in quite a similar manner to that observed in the model liquefaction tests shown in Fig. 2 (b), despite the difference in the fundamental mechanism.

Furthermore, another transient seepage analysis was implemented, wherein the water film is superposed to the pressure distributions obtained in the second step of the two-step analysis mentioned above, by suddenly changing permeability coefficient k_{wf} from 0.5×10^{-4} m/s to 1.0×10^{-1} m/s in those 0.15 m thin elements from $x = 0$ to 50 m at the start of the analysis, $t = 0$. This can supposedly simulate the formation of a water film at the top of the liquefied layer as soon as the full liquefaction has been attained. Fig. 6 (b) depicts pressure Δh, thus obtained, plotted versus depth z at $x = 50$ m (at the tip of the water film). The pressure is obviously different near the water film from the case in Fig. 6 (a). In Fig. 6 (c), the difference in depth-dependent pressure distributions reflecting the effect of the water film is singled out at $x = 50$ m by subtracting Fig. 6 (a-2) from Fig. 6 (b). This indicates that the head Δh at the tip tends to increase by $0.4 \sim 0.8$ m due to the existence of the water film for $t = 10 \sim 3600$ s. Although the timing of the Δh variations calculated here may occur earlier or later, depending on the assumed parameters, the resulting pressure variations are expected to correspond qualitatively with the observed in situ behavior.

Fig. 7 (a) plots the time-dependent variations in the excess pressure head obtained by the same calculation as that used for the full liquefaction accompanying the water film on semi-log graphs at depths of $z = 0$ to 5.0 m for $t = 0 \sim 3600$ s at $x = 50$ m. Fig. 7 (b) shows the results without the water film obtained from the same analysis, which has already been addressed in Fig. 6 (a-2) during liquefaction. The horizontal solid lines drawn in Fig. 7 (b) correspond to the initial excess pressure heads Δh given as the initial condition for full liquefaction at individual ground depths z. In actual liquefaction behavior, the excess pressures should stay constant as long as full liquefaction continues, while the calculated values in the transient seepage analysis

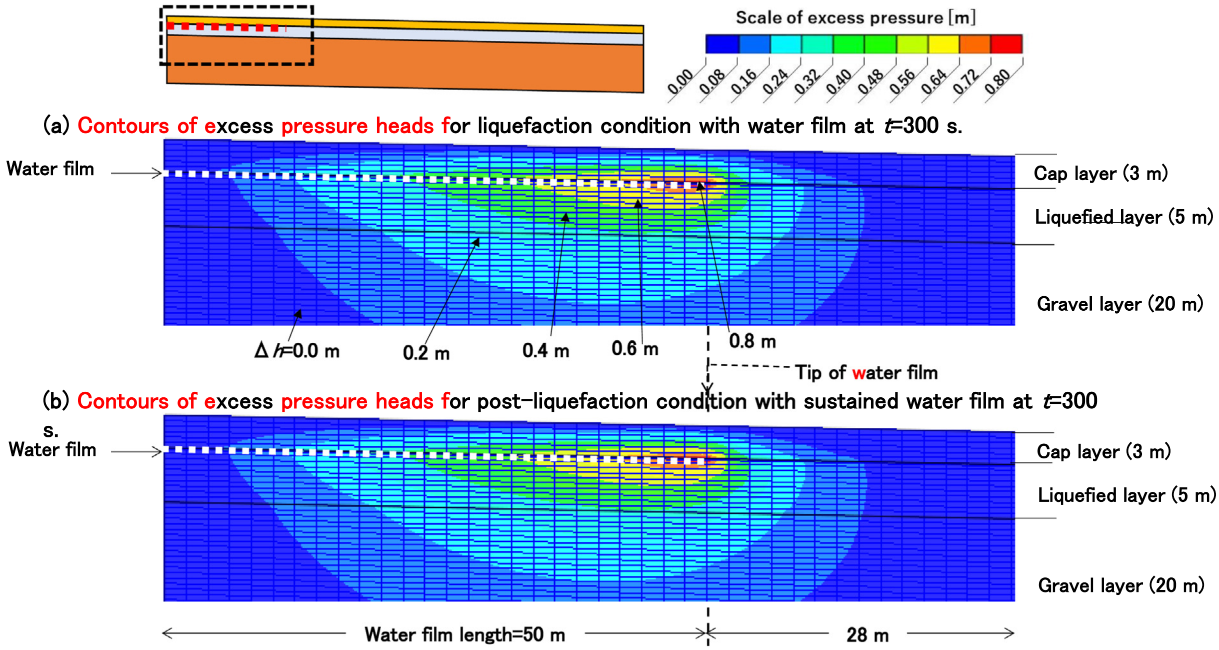

Fig. 8. Contours of excess pore pressure heads at $t = 300$ s around water film: (a) liquefaction condition with water film and (b) post-liquefaction condition with sustained water film.

tend to exceed them temporarily and then gradually decrease with time, except at deeper ground levels. A similar trend can also be seen in Fig. 7 (a) where the water film effect is incorporated at the beginning. Thus, the transient seepage analysis results deviated somewhat from true liquefaction behavior. The results in Fig. 7 (c) were obtained by subtracting (b) from (a) for the purpose of isolating the effect of the water film on the pressure distribution. This is because the background pressure, which deviates from actual liquefaction behavior due to the approximation in the transient seepage analysis performed here, may be effectively canceled out through the subtraction. According to Fig. 7 (c), the pressure head at $z = 3.0$ m tends to rise by 0.4 m in the first 10 s because of the existence of the water film and by 0.8 m in 100 s at the tip of the water film. Considering the 2 % gradient of the slope, the head loss of $\Delta h = 1.0$ m is expected during the steady state downslope flow of a horizontal distance of 50 m. Nevertheless, the head of 0.4 ~ 0.8 m is preserved without a large head loss because of the water film.

In Fig. 8 (a), contours of the excess pressure heads during liquefaction are provided with the water film at $t = 300$ s as the representative time section among others. It should be emphasized that the background pressure for the liquefaction is canceled out here, as was already mentioned. Obviously, the water film does raise the head by $\Delta h = 0.8$ m maximum at the tip and in the wide area along the water film. As mentioned above, the head of $\Delta h = 0.8$ m means that only 20 % out of the 1.0 m head is lost while the remaining 80 % is preserved. It is noted that the pressure head thus calculated around the front of the water film should be added to the excess pore pressure built up during full liquefaction in order to reach the absolute excess pressure head. The pressurized zone in Fig. 8 (a) tends to expand before and even beyond the tip, reflecting the strong effect of the water film which raises the pressure and supplies a large amount of seepage water to the surrounding soil. It also indicates that the effect does not stop at the tip of the water film, but extends beyond by more than 10 m downslope.

Fig. 9 (a) plots the time-dependent variations in the excess hydraulic gradient in the vertical direction, Δi_z, in the semi-log graph at depths of GL.0.0 to −5.0 m along the vertical line at $x = 50$ m (the tip of the water film). The gradient Δi_z is calculated here from excess pressure heads Δh_j and Δh_{j+1} in Fig. 7 (c), along the vertical line corresponding to vertical coordinates z_j and z_{j+1} as

$$\Delta i_z = -\left(\Delta h_j - \Delta h_{j+1}\right)/\left(z_j - z_{j+1}\right) \tag{9}$$

All the Δi_z-values are obtained positively in the cap layer above GL.-3.0 m ($z \geq 3.0$ m), indicating that the upward flow from the water film is dominant. In addition, it should be remembered that the liquefied Layer 2 and the cap Layer 1 are under a critical hydraulic gradient, expressed as $i_{cr} = (\rho_{sat} - \rho_w)/\rho_w$ in Eq. (6), which is canceled out in Fig. 9 (a) by the subtraction that was conducted to single out the water film effect. Consequently, the absolute vertical hydraulic gradient i_z, that is actually working in the soil layers, is obtained as $i_z = \Delta i_z + i_{cr}$ by adding $i_{cr} = 0.8$ to the values in Fig. 9 (a).

Fig. 10 (a) illustrates the contours of absolute vertical hydraulic gradient $i_z = \Delta i_z + 0.8$. Similar to the pressure contours in Fig. 7 (a), the gradients exceeding the critical value of $i_{cr} = 0.8$ are observed extensively in the cap layer

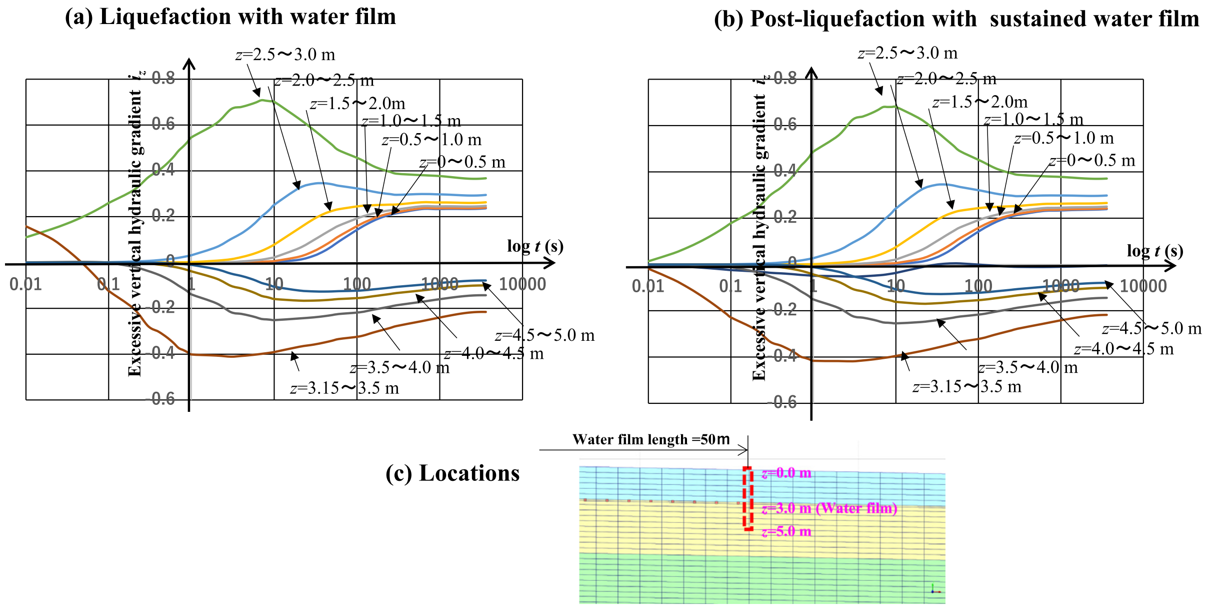

Fig. 9. Excessive vertical hydraulic gradients exceeding critical gradient i_{cr}=(ρ_{sat}-ρ_w)/ρ_w caused by existence of water film for t = 0 ∼3600 s obtained by transient flow analysis along vertical line of x = 50 m from GL.0.0 to −5.0 m: (a) during liquefaction with water film and (b) post-liquefaction with sustained water film.

above and beyond the water film tip. This indicates the significant potential for destabilizing the cap layer due to boiling near the tip, potentially causing the instability to progress farther downslope.

Fig. 11 (a) shows the time-dependent variations in horizontal seepage velocity v_x calculated along the water film near the tip x = 46 ∼ 54 m plotted versus time in the log–log graph. It is noted again that the background velocity in the liquefied ground is canceled out here to highlight the effect of the water film. The initial velocities are read off as $v_x = 2.0 \times 10^{-3}$ m/s and 1.0×10^{-6} m/s, matching those calculated by the simple equation $v_x = k_x \times i_x$ using the horizontal hydraulic gradient $i_x = 0.02$ where the horizontal permeability is $k_x = k_{wf} = 1 \times 10^{-1}$ m/s before the tip (x = 46 ∼ 50 m) and 0.5×10^{-4} m/s beyond it (x = 50 ∼ 54 m), respectively. Over tens or hundreds of seconds, however, the figure shows that the v_x within the water film decreases to approximately 1/10 at x = 46 ∼ 50 m (before the tip), while at x = 50 ∼ 54 (beyond the tip), it increases about tenfold. This suggests that water flowing through the water film at a higher seepage velocity will likely penetrate the tip, thereby extending the water film farther downslope.

Fig. 12 (a) depicts the distribution of the two-dimensional seepage velocity $(v_x^2 + v_z^2)^{0.5}$ plotted on the cross section of the slope at t = 300 s, wherein vertical velocity v_z, reflecting the water film, is very small. As for horizontal seepage velocities v_x, constant velocities of $v_{x1} = 0.1 \times 10^{-6}$ m/s, $v_{x2} = 1.0 \times 10^{-6}$ m/s, and $v_{x3} = 2.0 \times 10^{-6}$ m/s by the stationary downslope water flow are to be superposed in Layers 1, 2, and 3, respectively, in addition to the values in the figure. It is clearly shown that large velocities tend to concentrate in the water film from the left to the tip, where they drastically drop to smaller values beyond the tip. It is not difficult to imagine that a large volume of water flowing through the water film with a high-pressure head will try to penetrate weaker soils at the tip, thereby advancing the water film ahead.

(2) Transient Seepage Analysis for Post-Liquefaction Sustained Water Film

Similar calculations were also conducted for the post-liquefaction condition, wherein the depth-dependent excess pore pressure distribution of ADHCE in Fig. 4 (b) and Eq. (7) is initially given corresponding to the post-liquefaction condition where the water film is sustained after the end of liquefaction. Fig. 13 (a) depicts the depth-dependent distributions of the excess pressure thus calculated by the transient seepage analysis for t = 0 ∼3600 s at x = 50 m. It should be mentioned that the pressure distributions were obtained identically by the two-step procedure in a similar manner to that for the full liquefaction case shown in Fig. 6. In Fig. 13 (b), the same calculation is implemented again, except that the water film is superposed by abruptly changing the permeability coefficient from $k_{wf} = 0.5 \times 10^{-4}$ m/s to 1×10^{-1} m/s at the beginning of the transient seepage analysis. The subtraction of (b) from (a) in Fig. 13 (c) singles out the effect of the sustained water film on the excess pore pressure at x = 50 m under the post-liquefaction sustained water film condition.

It is noted here that the results in Fig. 13 (c) are almost identical to those in Fig. 6 (c) despite the clear difference in initial pressure distributions corresponding to either the full liquefaction condition or the post-liquefaction residual water film condition. This indicates that the numerical procedure employed here in the transient seepage analysis,

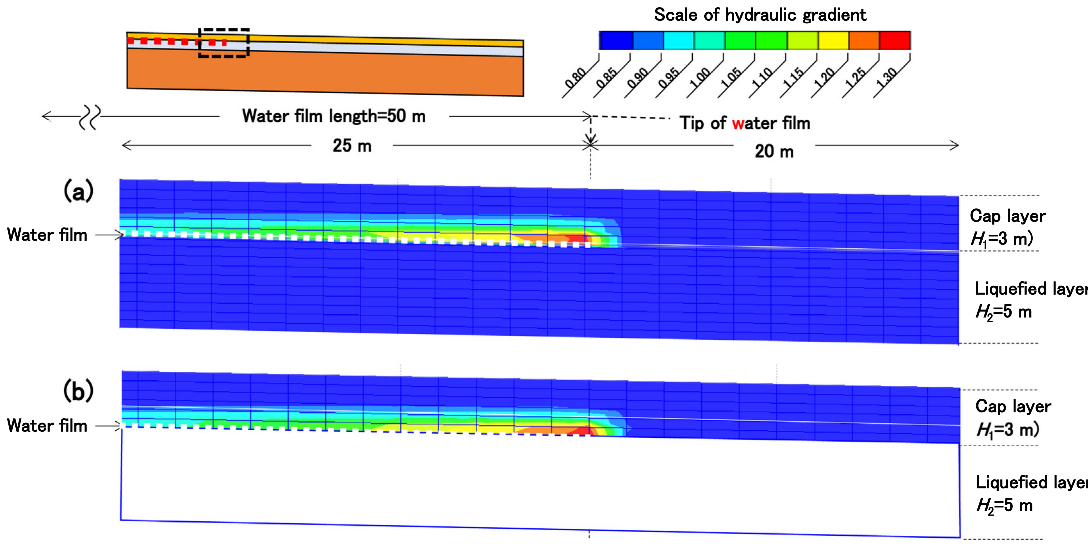

Fig. 10. Contours of absolute hydraulic gradient due to emerging water film at $t = 10$ s: (a) during liquefaction with water film and (b) post-liquefaction with sustained water film.

superposing the initial pressure distribution and the instantaneous change in permeability corresponding to the water film emergence, seems to be functioning almost as a linear system, for which the principle of superposition holds; and hence, the same solution can be singled out as the effect of the water film formation regardless of the background pressure distributions in the model.

In Fig. 8 (b), the excess pressure head increments due to the sustained water film are calculated and illustrated in the contour graph for $t = 300$ s. They are identical to those in Fig. 8 (a), indicating again that the difference in the distributions of initial pore pressures given to the model for full liquefaction in Eq. (5) and post-liquefaction with sustained water film in Eq. (7) has no impact on the spatial pressure variation caused by the existence of the water film. The excessive vertical hydraulic gradient, due to the water film, is accordingly calculated from the pressure increment, as shown in Fig. 9 (b), and found again to be identical to the case for liquefaction with the water film in Fig. 9 (a). The contour of the absolute vertical hydraulic gradient of i_z at $t = 300$ s is also depicted in Fig. 10 (b), wherein $i_z =$-$\Delta i_z + i_{cr} = \Delta i_z + 0.8$ in the cap layer and $i_z = \Delta i_z$ in the sand layer after the liquefaction has subsided. Once again, i_z in the cap layer is recognized as being visually the same as that in Fig. 10 (a).

The horizontal seepage velocity in the residual water film under the post-liquefaction condition is also calculated and depicted versus time in Fig. 11 (b), which has been found to be identical to that in Fig. 11 (a), already calculated for the water film during liquefaction. The seepage velocity distributions around the water film, at $t = 300$ s, are also calculated in Fig. 12 (b) almost identically as the case of full liquefaction with the water film. Hence, the same observations as before may be possible, namely, that the water film tends to increase the slope instability around its tip whether the soil is liquefied or not, as long as the water film is sustained.

6. Discussions

In this paper, simplified transient seepage analyses with specific initial conditions have been conducted to approximate the processes of liquefaction and water film generation, as already mentioned. This is because getting a reliable solution by a rigorous numerical analysis, incorporating liquefaction-induced water films considering slope sliding, seems beyond the present state of the art in numerical analyses. The approximation method employed here seems to have successfully replicated the pressure distribution during liquefaction which serves as background pressure to single out the effect of a water film. It was also found in the analyses that the difference in background pressures between the full liquefaction and the post-liquefaction, with the residual water film initially given in Eq. (5) and Eq. (7), respectively, makes literally no difference in terms of the effect of the water film on the pressure, hydraulic gradient, or seepage velocity. Hence, it may be justified to assume that the effect of a water film on the pressure distribution, once formed during liquefaction, is similarly sustained as long as it also remains steady during and after liquefaction under actual field conditions.

In these analyses, the length of the continuous water film L_{wf} is tentatively assumed as 50 m. L_{wf} is considered an influential parameter for determining the degree of instability, although this value may not be so unrealistic in the slope failures in Palu. As L_{wf} becomes longer under the same slope gradient, the pressure head working at the water film front tends to be higher, causing a higher potential for boiling failure due to a higher vertical hydraulic gradient. It also induces a higher horizontal hydraulic gra-

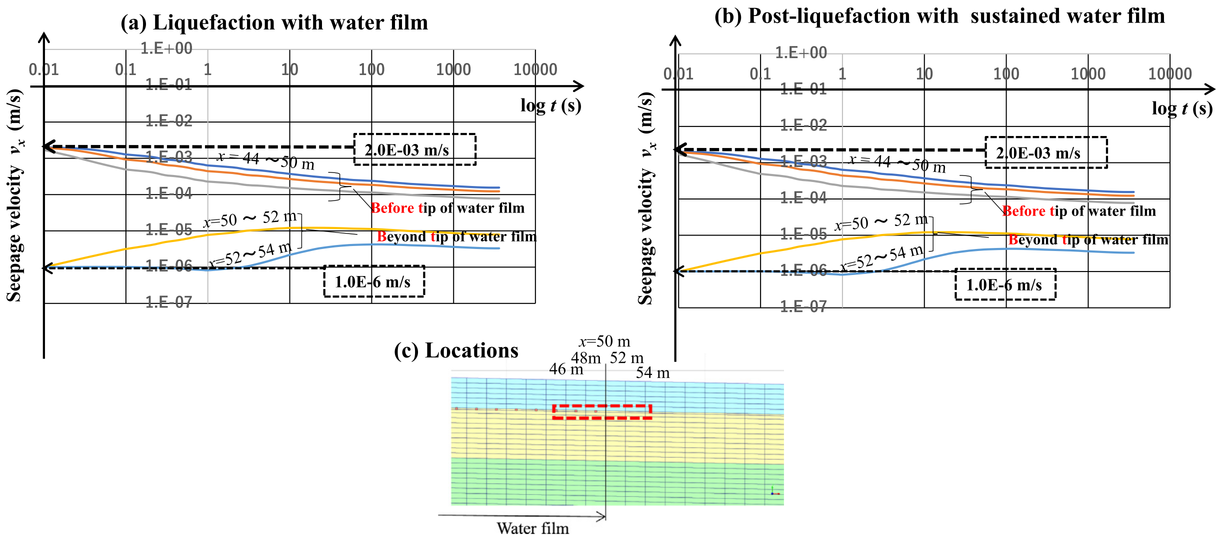

Fig. 11. Horizontal seepage velocity in water film for $t = 0 \sim 3600$ s obtained by transient flow analysis: (a) during liquefaction with water film and (b) post-liquefaction with sustained water film.

dient in front of the water film which will help the water film advance farther in front. The equivalent permeability of the water film may be another influential parameter in determining its effect. The seepage water volume will rise drastically with the increase in permeability which is assumed here conservatively as $k_{wf} = 1.0 \times 10^{-1}$ m/s.

In conclusion, the series of transient seepage analyses indicated that once a water film has formed during liquefaction, a slope subjected to steady seepage flow may become destabilized due to excessive pressure surges, hydraulic gradients, and significant water flow volumes at or near the water film tip. Water films act as conduits, allowing seepage water to flow with minimal head loss, thereby increasing the water head near the lower end of the water films compared to conditions without water films. This elevated head can lead to boiling failures in the cap layer above the tip. However, if boiling occurs, it may reduce the pressure head and partially mitigate the destabilizing effect. This phenomenon was observed in the video of the Jono Oge slide, where boiling at the ground surface occurred selectively at a downslope portion, although it did not significantly disrupt the overall flow movement.

Additionally, the increased water head may facilitate the sequential development of water films in front of intensely sheared soil zones. The extent of the slope destabilization caused by shearing near the tips of water films depends on various soil properties, such as density, fines content, and plasticity. Although this paper does not explore this aspect, it is worth noting that the soils in Palu appeared to be more prone to destabilization due to their specific characteristics of low to medium density, high fines content, and low or no plasticity (JICA 2019).

Finally, the artesian pressure observed locally at several points of the slopes may have reduced the effective vertical stress by increasing the vertical hydraulic gradient even before the earthquake and assisted liquefaction to occur more easily during the earthquake. However, it seems unclear how the local artesian pressure could have triggered widespread boiling over the long slopes during the earthquake and serve as a key mechanism of the continuous flow longer than hundreds of meters without the involvement of water films.

Consequently, water films during liquefaction under the effect of stationary seepage flow are critical in realizing long-distance flow failures of gentle slopes. Liquefaction is firstly needed to generate water films, although it is not an essential requirement for the failures once the water films have formed, as long as they are sustained even after the liquefaction has subsided.

7. Summary

To elucidate the fundamental mechanism behind the unprecedented long-distance flows on gentle slopes caused by earthquake-induced liquefaction during the 2018 Sulawesi earthquake in Indonesia, transient seepage analyses were conducted on a simplified slope model with a gradient of 2 %, influenced by stationary downslope seepage that flowed continuously even before the earthquake. As the key of the mechanism, a liquefaction-induced 0.15-m thin water film, 50 m in length, was supposed to emerge in the model at the top of a 5-m-thick liquefied layer beneath a 3-m-thick low-permeable cap layer, yielding the following findings.

1) The transient seepage analysis of the slope model, although different in its basic mechanism from a non-linear analysis on liquefaction-induced excess pore pressure buildup, was found to be able to approximate the pressure change for full liquefaction and

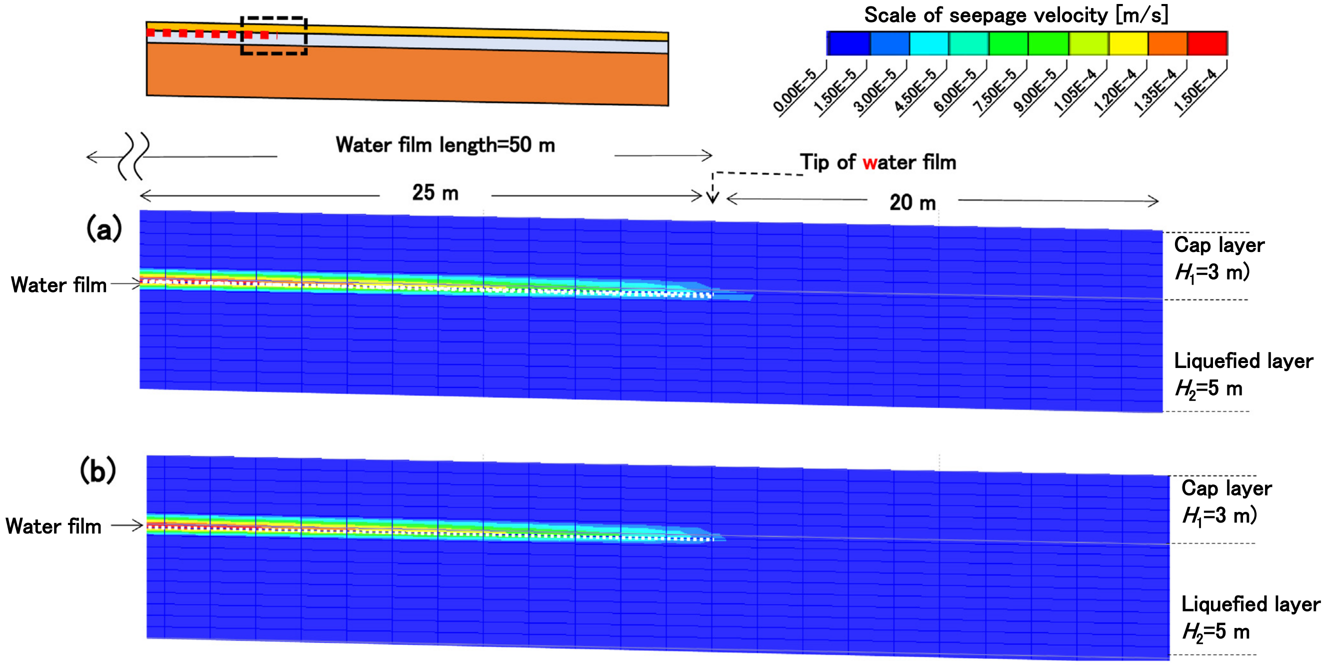

Fig. 12. Seepage velocity contours around water film due to emerging water film at t = 300 s: (a) during liquefaction with water film and (b) post-liquefaction with sustained water film.

subsequent post-liquefaction conditions if the initial and boundary conditions are assumed appropriately.

2) Two transient seepage calculations were conducted with and without a water film, under otherwise exactly the same conditions, by employing the calculated pressure change as the background pressure. Pressure head increments Δh, caused by the generation of the water film in the slope under the effect of stationary downslope water flow, were isolated by subtracting the former from the latter. This subtraction allowed for the cancellation of the unfavorable results from the approximated transient seepage analysis, which may not have precisely simulated the actual liquefaction behavior.

3) The pressure head increments Δh, thus calculated, tended to concentrate around the tip of the water film with the maximum value of Δh = 0.8 m out of the total head of Δh = 1.0 m with minimal (20 %) head loss, which became possible due to the smooth water flow in the thin (0.15 m) water film with a length of 50 m in the slope with a gradient of 2 %.

4) It was found that increments in the pressure head, the associated hydraulic gradients, and the large seepage velocity caused by the thin water film will be critical for destabilizing gentle slopes by boiling in the cap layer above the tip and extending the water film in the front.

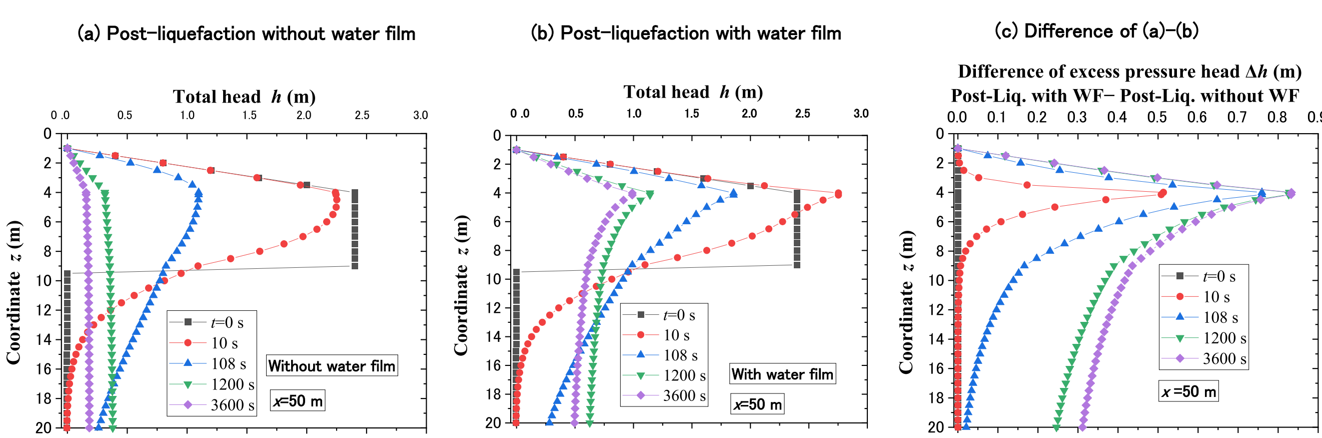

Fig. 13. Depth-dependent distributions of excess pressure heads by transient flow analysis by initial pressure corresponding to sustained water film at x = 50 m: (a) without water film, (b) with water film, and (c) (b)-(a) at x = 50 m.

5) The emergence of water films under stationary seepage flow is the key to realizing the long-distance flow failure of very gentle slopes. Liquefaction is needed to generate the water films first, although it is not an essential requirement for failure as long as the water films are sustained under post-liquefaction conditions.
6) Thus, the significant role of liquefaction-induced water films in gentle slopes under stationary seepage flow has been shown in the simplified analyses presented here. This type of failure, which is not yet well known, should be recognized as a serious geotechnical hazard because it may develop into devastating long-distance flow slides.

As a future study to approach more detailed field behavior, advanced numerical schemes employing discrete element methods or particle hydrodynamics need to be developed which can deal with large-strain liquefaction-induced settlement including the formation of water films combined with soil–water interaction for the long-distance flows of soil–water mixtures.

CRediT authorship contribution statement

T. Kokusho: Writing – review & editing, Writing – original draft, Visualization, Validation, Supervision, Project administration, Methodology, Investigation, Formal analysis, Data curation, Conceptualization. **T. Sawada:** Software, Formal analysis, Data curation. **H. Hazarika:** Writing – review & editing, Project administration, Conceptualization. **Y. Isobe:** Writing – review & editing, Resources, Project administration, Methodology, Funding acquisition.

Acknowledgments

The authors gratefully acknowledge JICA (Japan International Corporation Agency) for providing a variety of information and support in visiting the damaged sites to investigate the slope failures. The authors also express their sincere gratitude to the members of the JICA domestic committee in Japan chaired by Prof. Kenji Ishihara for valuable comments and discussions on slope failure mechanisms. Particular thanks are extended to Professor Takashi Kiyota, the University of Tokyo, Professor Mitsu Okamura, Ehime University, as well as Dr. Hisashi Furuichi, Yachiyo Engineering Co., Ltd., Japan for the valuable information they provided on the site investigation studies. Lastly, the authors acknowledge the financial support for this research under the Japan Society for Promotion of Science (JSPS) KAKENHI (Grant Number: 20H02244; Principal Investigator: Hemanta Hazarika).

References

Akai, K., Ohnishi, Y., Nishigaki, M., 1977. Finite element analysis of saturated – unsaturated seepage in soil. J. Japan Society Civil Eng. 264, 87–96.

Akai, K., Ohnishi, Y., Nishigaki, M., 1979. Finite element analysis of three dimensional flows in saturated – unsaturated soils. Third International Conference on Numerical Methods in Geomechanics, 227–239.

Boulanger, R.W., Truman, S.P., 1996. Void redistribution in sand under post-earthquake loading. Canadian Geotech. J., 33, 829–833.

Hazarika, H., Rohit, D., Pasha, S.M.K., Maeda, T., Masyhur, I., Arsyad, A., Nurdin, S., 2020. Large distance flow-slide at Jono-Oge due to the 2018 Sulawesi earthquake, Indonesia. Soils Found. 61 (1), 239–255.

JICA, 2019. Report of the technical committee on the 2018 Sulawesi earthquake, Indonesia, Japan International Corporation Agency (in Japanese).

Kabasawa, K., Kokusho, T., 2004. Energy analysis and model tests on lateral flow induced by water film effect in liquefied ground. J. JSCE, Japan Civil Eng. Society 771 (III-68), 135–145 (in Japanese).

Kiyota, T., Furuichi, H., Hidayat, R.F., Tada, N., Nawir, H., 2020. Overview of long-distance flow-slide caused by the 2018 Sulawesi earthquake, Indonesia. Soils Foundat. https://doi.org/10.1016/j.sandf.2020.03.015.

Kokusho, T., 2000. Mechanism for water film generation and lateral flow in liquefied sand layer. Soils Found. 40 (5), 99–111.

Kokusho, T., Kojima, T., 2002. Mechanism for postliquefaction water film generation in layered sand. J. Geotechn. Geoenviron. Eng., Am. Society Civ. Eng. 128 (2), 129–137.

Kokusho, T., Fujita, K., 2002. Site investigation for involvement of water films in lateral flow in liquefied ground. J. Geotechn. Geoenviron. Eng., Am. Society Civ. Eng. 128 (11), 917–925.

Kokusho, T., 2003. Current state of research on flow failure considering void redistribution in liquefied deposits, Soil Dynamics and Earthquake Engineering, Elsevier, 23, 585–603.

Kokusho, T., 2017. Innovative earthquake soil dynamics. CRC Press, Taylor and Francis Group.

Kulasingam, R., Malvick, E.J., Boulanger, R.W., Kutter, B.L., 2004. Strength loss and localization at silt interlayers in slopes of liquefied sand. J. Geotech. Geoenviron. Eng. ASCE 130 (11), 1192–1202.

Malvick, E.J., Kutter, B.L., Boulanger, R.W., Kabasawa, K., Kokusho, T., 2005. Void redistribution research with 1-g and centrifuge modeling. Proc International Conference on SMGE.

NRC (National Research Council), 1985. Liquefaction of soils during earthquakes, Committee of Earthquake Engineering, Commission of Engineering and Technical Systems, National Academy Press, Washington, D.C.

Mason, H.B. et al. (18 co-authors), 2021. East Palu Valley flowslides induced by the 2018 M_W 7.5 Palu-Donggala earthquake, Geomorphology, Elsevier, Volume 373, 15.107482.

Okamura, M., Ono, K., Minaka, U.S., Arsyad, A., Nurdin, S., 2020. Large scale flow side in Sibalaya - A consequence of the 2018 Sulawesi Earthquake, Indonesia. Soils Found. 60 (4), 1050–1063.

Rohit, D., Hazarika, H., Maeda, T., Sumartini, W.O., Kokusho, T., Pasha, S.M.K., Nurdin, S., 2021. Forensic investigation of flow slides triggered by the 2018 Sulawesi earthquake. Prog Earth Planet Sci 8 (1), 1–20. https://doi.org/10.1186/s40645-021-00452-5.

Rohit, D., Hazarika, H., Qin, C., Maeda, T., Kokusho, T., Yahiro, Y., Prabhakaran, A., 2023. Simulation of water film formation during the 2018 Sulawesi earthquake. Indonesia, Forensic Engineering 176 (4), 119–133.